Chen et al., https://doi.org/10.1083/jcb.201604025

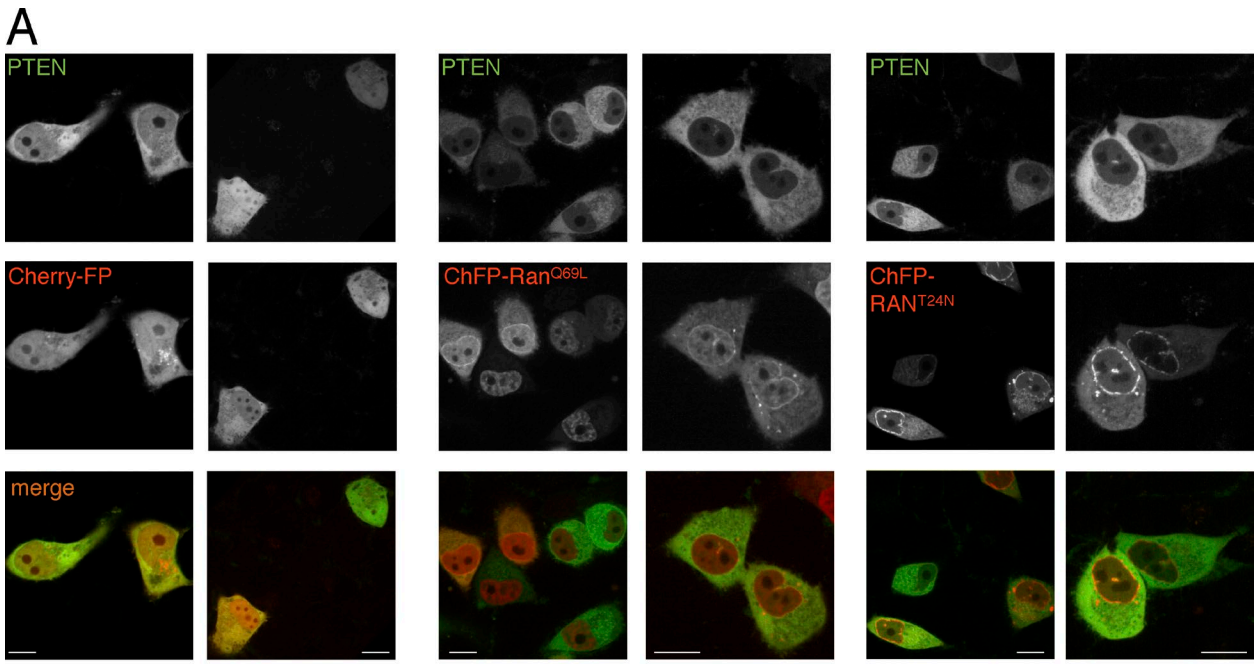

C

		Relative Results		Absolute Results		
		nuclear & cytoplasmic	nuclear excluded	nuclear & cytoplasmic	nuclear excluded	cell number
ΔN-IPO11 positive	chFP-PTEN	17%	83%	9	45	54
GFP-positive	chFP-PTEN	83%	17%	57	12	69
		nuclear	cytoplasmic	nuclear	cytoplasmic	
ΔN-IPO11 - positive cells	p27	83%	17%	128	27	155
	E2E3	5%	95%	7	148	155
ΔN-IPO11 - negative cells	p27	83%	17%	131	26	157
	E2E3	82%	18%	129	28	157

Figure S1. **Pten nuclear import is Ran dependent.** (A) Effects of the RAN^{Q69L} and RAN^{T24N} mutants (mCherry-FP tagged) on exogenous GFP-PTEN localization. Biological replicates (n_{biol}) = 2. Bars, 10 µm. (B) Domain organization of IPO11 and the derived constructs used in this study. (C) Relative and absolute counts of protein localizations that were scored in experiments from Fig. 1 C.

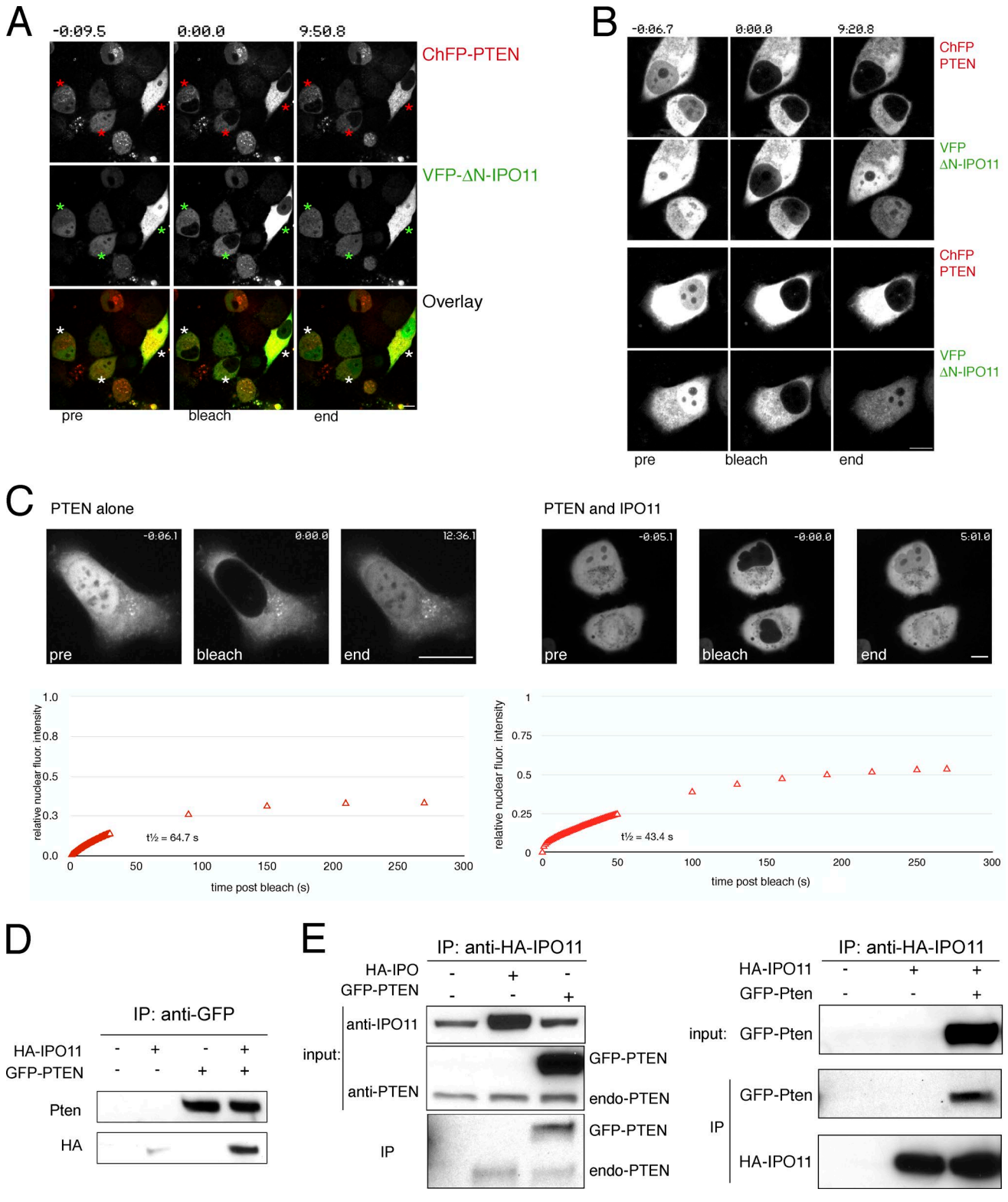

Figure S2. **PTEN nuclear import is blocked by a dominant-negative mutant of IPO11.** (A) Wide-field image of FRAP analysis shown in Fig. 1 E shows consistent effects in bleached high- and low-expressing cells: absence of ChFP-PTEN recovery (red asterisks) and efficient VFP-ΔN–IPO11 recovery (green asterisks; see also white asterisks in overlay). Time stamps (m:ss.s) relative to bleach point are indicated. Bar, 10 µm. (B) ChFP-PTEN transport block (and VFP-ΔN–IPO11 recovery after bleaching) are independent of cell size. Time stamps (m:ss.s) are indicated. Bar, 10 µm. (C, top) FRAP assay showing typical images of ChFP-PTEN cells at prebleach, bleach, and experimental endpoints. Time stamps (m:ss.s) relative to bleach point are indicated. (bottom) Recovery of mean nuclear fluorescence intensity over time. Bars, 10 µm. Biological replicates (n_{biol}) = 4. (D and E) Reciprocal coIPs of IPO11 and PTEN show that IPO11 can form a complex with PTEN in HEK293 cells and that the HA-tag IP is very efficient. n_{biol} = 2.

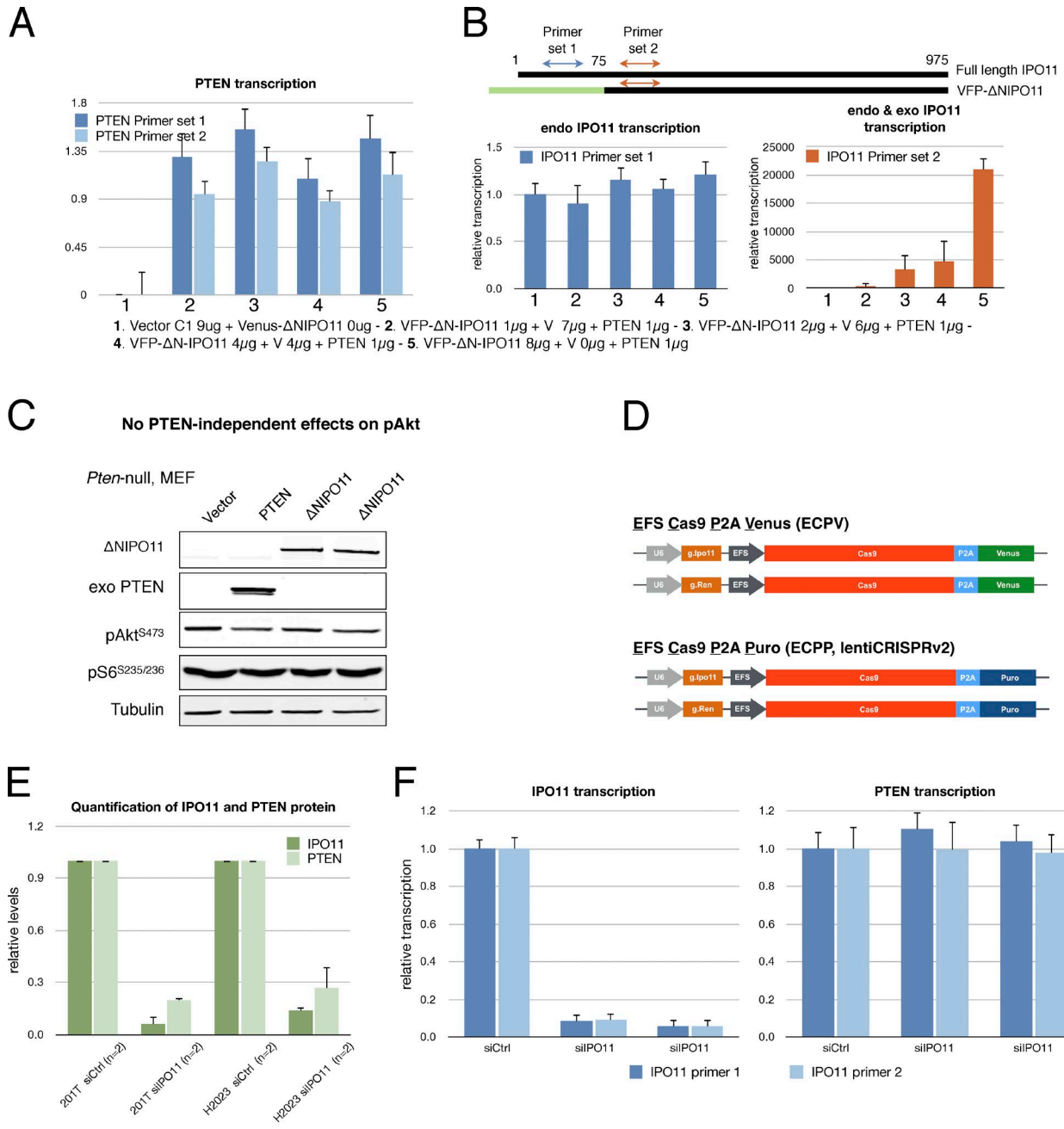

Figure S3. **Validation of transgenic, knockdown, and knockout tools.** (A) qRT-PCR of *Pten* mRNA levels. Error bars are SD of experimental triplicates. Biological replicates (n_{biol}) = 2. (B) qRT-PCR of endogenous *IPO11* (blue columns and blue amplicon) and overexpressed VFP-ΔN–IPO11 (orange columns and orange amplicon) in samples from Fig. 2 C as indicated. Note that endogenous IPO11 RNA remained constant in these cells. Error bars are SD of triplicates; n_{biol} = 2. (C) The mutant IPO11 (VFP-ΔN–IPO11) does not affect p-AKT pathway signaling in the absence of PTEN, as seen in *Pten*-null MEFs; n_{biol} = 2. Biological replicates are shown in lanes 3 and 4. (D) Schematic of lentiviral plasmids used for CRISPR-Cas9 knocking out of *Ipo11/IPO11*. We developed plasmid carrying fluorescent protein Venus for in vivo delivery to prostate. ECPV plasmid was derived from lentiCRISPRv2 (see Materials and methods) and is called ECPP in this study to keep the nomenclature clear. (E) Quantification of IPO11 and PTEN protein. Error bars are SD of experimental duplicates; n_{biol} = 2. (F) qRT-PCR of *IPO11* and *PTEN* transcripts shows siRNA target effect on IPO11 and no off-target effect on *PTEN* mRNA. Error bars are SD of experimental triplicates; n_{biol} = 2.

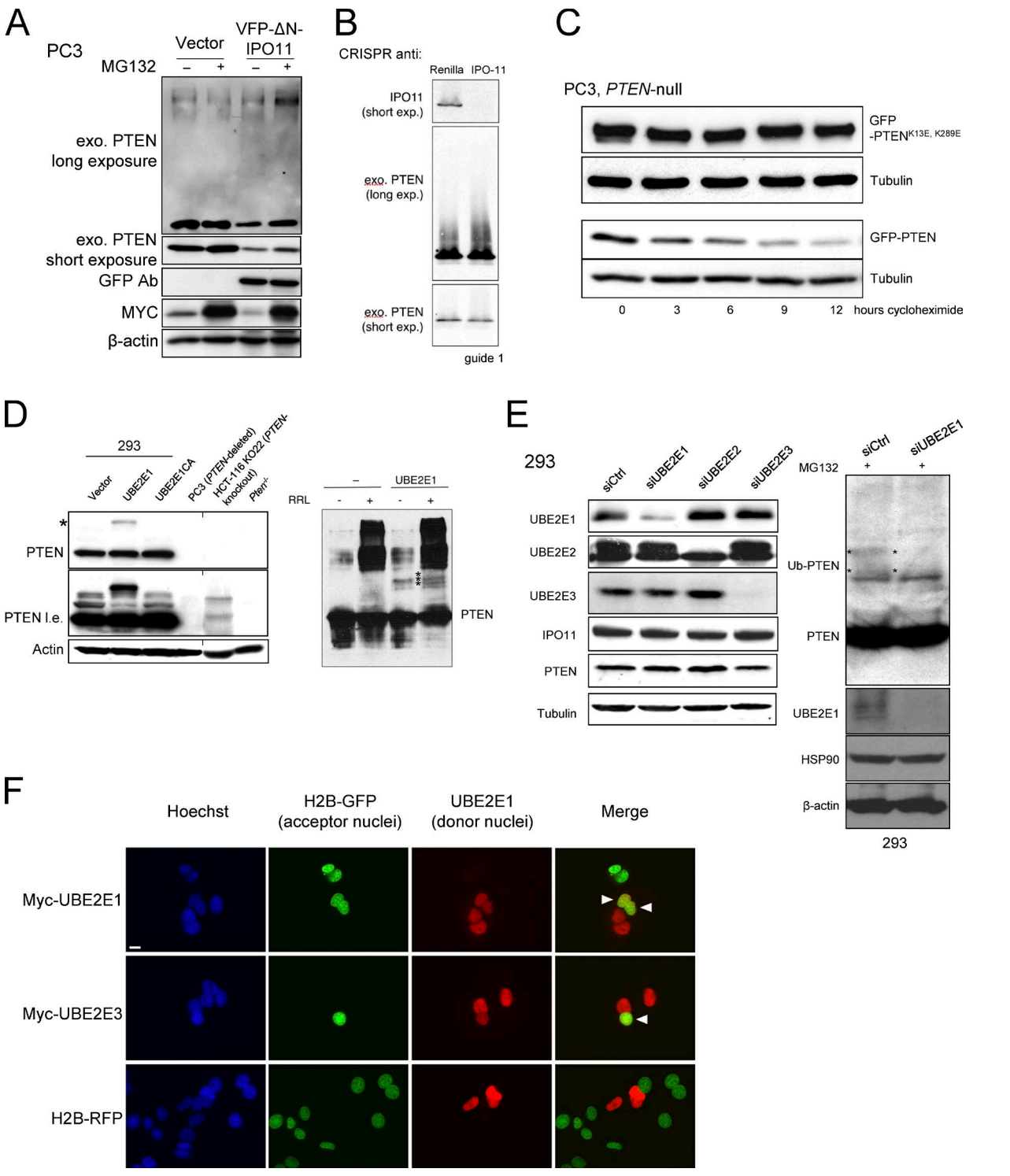

Figure S4. **Functional analysis of UBE2E1 perturbation.** (A) MG132-mediated proteasome inhibition reveals increase in overexposed PTEN adducts smear upon knockout of *IPO11* in PC3 cells. (B) MG132-mediated proteasome inhibition reveals increase in high molecular PTEN adducts upon VFP-ΔN–IPO11 overexpression (Pten long exposure [l.e.]) in PC3 cells (biological replicates [n_{biol}] = 2). MYC stability is shown as positive control for inhibition of degradation. (C) GFP-PTEN$^{K13E, K289E}$ $t_{1/2}$ after cycloheximide treatment is extended compared with that of GFP-PTEN; n_{biol} = 2. (D, left) Antibody specificity shown by Western blot of PTEN, cotransfected with UBE2E1 as indicated and run next to three *PTEN* null cell lines: PC3 (prostate), HCT-116 KO22 (colon cell line with *PTEN* knockout), and *Pten*$^{-/-}$;*Trp53*$^{-/-}$ MEFs; n_{biol} = 3. A black line indicates splicing of an unrelated column. (right) In vitro ubiquitination assay using recombinant PTEN and UBE2E1 and rabbit reticulocyte lysate (RRL) as source for E3 ligases. Note UBE2E1-specific adducts indicated by asterisks. (E, left) Knockdown specificity, efficiency, and antibody specificity as shown by Western blotting of HEK293 cells after siRNA knockdown of UBE2E1, UBE2E2, and UBE2E3, respectively. (right) Knockdown of UBE2E1 combined with 6-h proteasome inhibition with MG132 reveals reduced ubiquitination of PTEN. Asterisks denote adduct bands. (F) UBE2E1 constitutively shuttles in and out of the nucleus. HeLa cells stably expressing histone H2B-GFP were mixed and seeded together with HeLa cells previously transfected with plasmids encoding Myc-UBE2E1, Myc-UBE2E3, or histone H2B-RFP. The H2B-GFP nuclei serve as acceptors, as the fusion protein does not shuttle, whereas the Myc-positive nuclei are donors. After polyethylene glycol–mediated fusion and a 2-h incubation, shuttling is seen as colocalization with H2B-GFP for the Myc-tagged proteins (arrowheads) but not for Histone H2B. Bar, 10 µm.

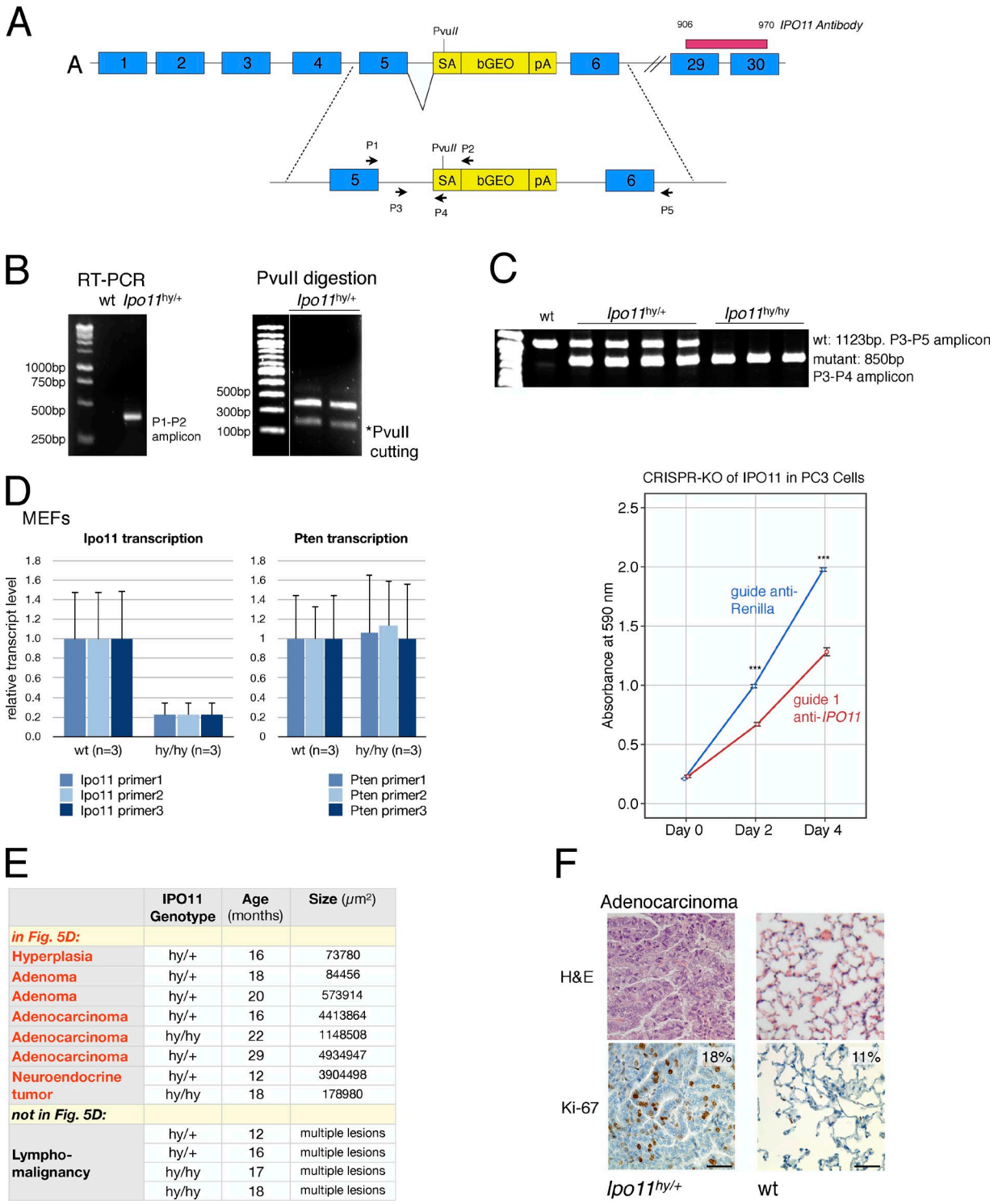

	IPO11 Genotype	Age (months)	Size (μm^2)
in Fig. 5D:			
Hyperplasia	hy/+	16	73780
Adenoma	hy/+	18	84456
Adenoma	hy/+	20	573914
Adenocarcinoma	hy/+	16	4413864
Adenocarcinoma	hy/hy	22	1148508
Adenocarcinoma	hy/+	29	4934947
Neuroendocrine tumor	hy/+	12	3904498
	hy/hy	18	178980
not in Fig. 5D:			
Lympho-malignancy	hy/+	12	multiple lesions
	hy/+	16	multiple lesions
	hy/hy	17	multiple lesions
	hy/hy	18	multiple lesions

Figure S5. **Genetic engineering and analysis of the *Ipo11* gene trap mouse.** (A) Map of *Ipo11* locus with the insertion of the gene trap vector in intron 5. The genomic sequence is depicted as a black line, with blue boxes representing exons 1–30. The yellow box represents the splice acceptor (SA) βGEO gene trap vector. Location of RT-PCR (P1 and P2) and genotyping primers (P3–P5) are shown with arrows. A red bar indicates the region used to generate the IPO11 antibody. (B) RT-PCR of RRU483 ES cells confirms insertion of the βGEO vector in intron 5 of the Ipo11 using P1 and P2 primers and PvuII digest. A white line in the right panel indicates splicing of an unrelated column. (C) Genotyping of mice derived from RRU483 ES cells reveals presence of wt and/or hy alleles after PCR with P3, P4, and P5 primers. (D, left) qRT-PCR of *Ipo11 and Pten* mRNA levels in MEFs from the indicated genotypes reveals that the SA-βGEO insertion into the *Ipo11* locus creates a strong hy allele that does not, however, affect Pten transcription. Error bars are SD of experimental triplicates. Biological replicates (n_{biol}) = 3. (right) Growth curves for IPO11 knockout and control-knockout (KO) PC3 cells, which are deficient of PTEN, reveal no growth advantage (rather a disadvantage) after *IPO11* loss. Error bars are SD of experimental triplicates; n_{biol} = 3. (E) Summary table of the lung lesions and sizes (as judged by μm^2 on H&E slides; see Fig. S6 A) observed in the *Ipo11* mutant mice. Lesions marked in red type were included in the Kaplan–Meier survival curve shown in Fig. 5 B. (F) Microscopic analysis reveals lung adenocarcinoma in a 16-mo-old *Ipo11*$^{hy/+}$ mouse. Quantification of cell proliferation was calculated using percent-positive Ki-67 IHC staining cells (see Materials and methods). Significance: adenocarcinoma – wt: P = 0.023. Bars, 50 µm.

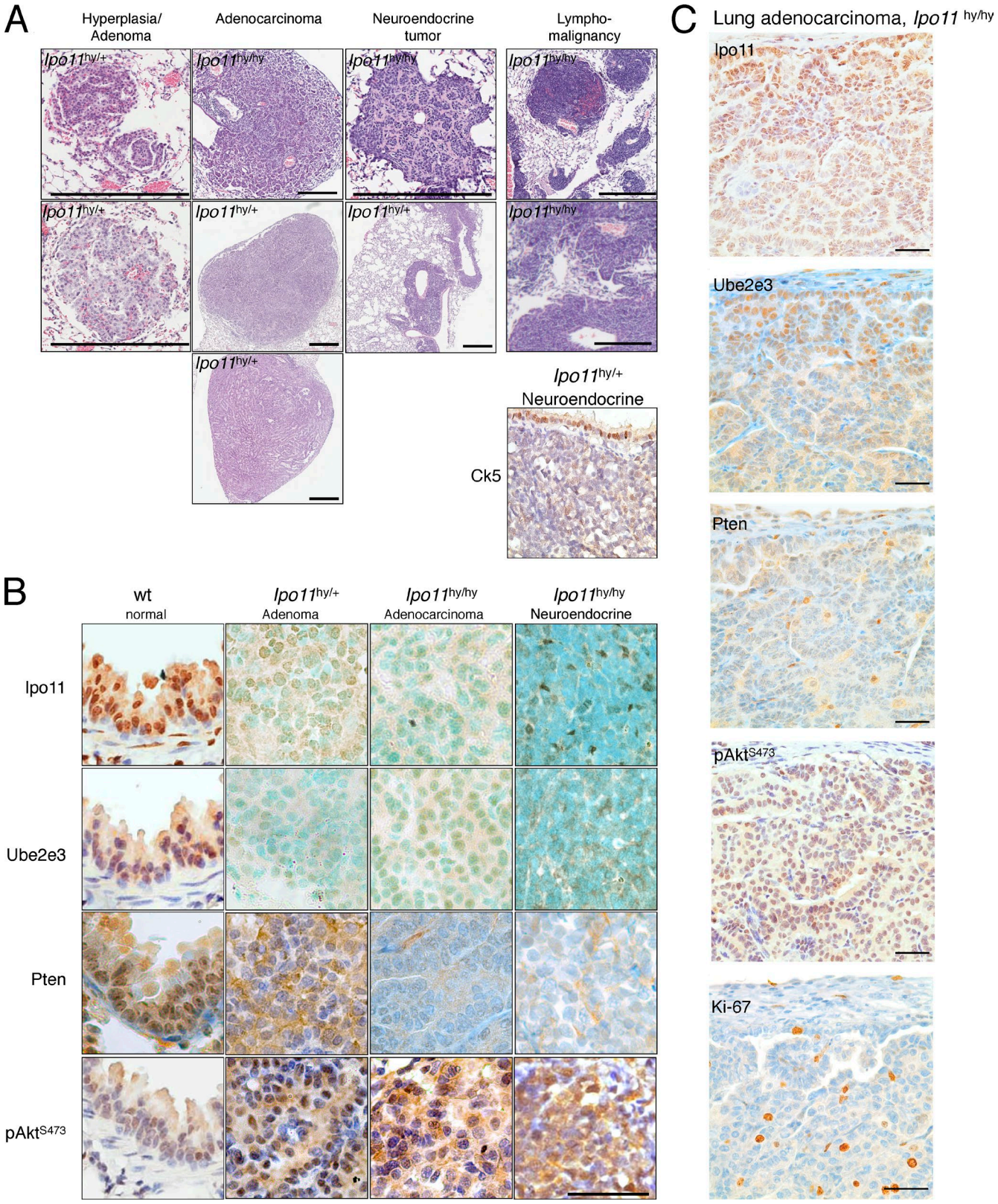

Figure S6. **Histopathology analysis ofmalignancy in the *Ipo11* gene trap mouse.** (A) Histopathology analysis reveals lung hyperplasia, adenoma, adenocarcinoma, neuroendocrine cancer, and lymphomalignancy in *Ipo11* mutant mice of the indicated genotypes (see also Fig. S5 E). (bottom right) Cytokeratin 5 (Ck5) staining of neuroendocrine cancer. Bars, 500 µm. (B) Comparative IHC analysis reveals the correlation of reduced (nuclear) Ipo11 levels in the indicated *Ipo11* mutant lung lesions with cytoplasmic mislocalization and reduction of Ube2e3 as functional readout of Ipo11 malfunction and with cytoplasmic mislocalization and reduction of Pten and activation of Akt. Note that methyl green (instead of hematoxylin) was used as nuclear counterstain in mutants with Ipo11 and Ube2e3 staining to reveal the faint remaining nuclear staining of Ipo11 and Ube2e3. Bar, 50 µm. (C) IHC analysis of Ipo11, Pten, Ube2e3, p-Akt, and Ki-67 in lung adenocarcinoma from a 16-mo-old *Ipo11hy/+* mouse. Bars, 50 µm.

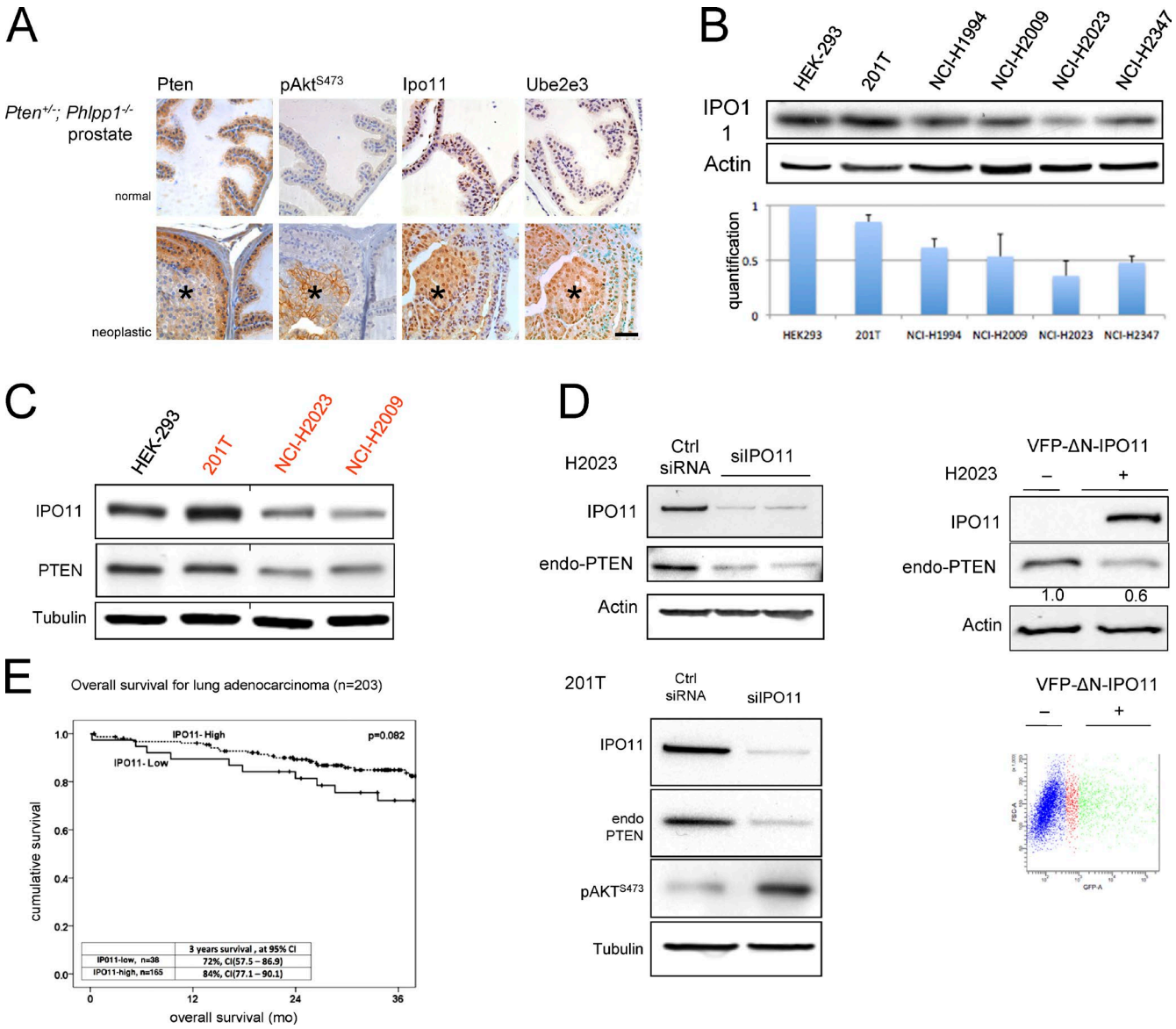

Figure S7. **Correlation of IPO11 and PTEN in cells, mouse prostate, and human lung cancer.** (A) Top panels show typical levels and localization of indicated proteins in phenotypically normal prostate of *Pten*$^{+/-}$; *Phlpp1*$^{-/-}$ mice. Bottom panels show the correlation among spontaneous reduction of Pten protein, Akt activation, and Ipo11 dysfunction as inferred from Ube2e3 mislocalization (asterisks). Bar, 50 µm. (B) Western blot and quantification of IPO11 levels in human lung cancer cell lines compared with HEK293 cells. Biological replicates (n_{biol}) = 3. (C) Western blotting reveals correlation of IPO11 and PTEN levels in 201T, NCI-H2023, and NCI-H2009 lung cancer cell lines (red) and in HEK293 (black). A black line indicates splicing of a column with a cell line that is otherwise irrelevant to this study. (D) *IPO11* knockdown suppresses endogenous PTEN levels in the IPO11 NCI-H2023 and 201T lung cancer cells; n_{biol} = 3. (left) Dominant-negative VFP-ΔN–IPO11 suppresses endogenous PTEN in the FACS-sorted VFP-positive NCI-H2023 lung cancer cells; n_{biol} = 3 (right). (E) Kaplan–Meier analysis of overall survival of 203 patients with lung adenocarcinoma. Patients with low IPO11 protein show a strong trend to worse overall survival than those with tumors that retain high IPO11.